NJC

ROYAL SOCIETY OF CHEMISTRY

PAPER

View Article Online
View Journal | View Issue

Cite this: *New J. Chem.*, 2022, **46**, 18890

A carboxylate- and pyridine-based organic anode material for K-ion batteries†

Kathryn Holguin,[a] Kaiqiang Qin,[a] Jinghao Huang[a] and Chao Luo *[ab]

Received 13th July 2022,
Accepted 6th September 2022

DOI: 10.1039/d2nj03447f

rsc.li/njc

Developing high-capacity, stable, and sustainable K-ion batteries (KIBs) is an ongoing challenge due to the lack of high-performance and environmentally benign electrode materials. To address this challenge, organic electrode materials that are affordable, abundant, highly sustainable, highly tunable and flexible offer opportunities. Herein, we report a novel N-containing carboxylate salt, $K_2C_{12}H_6N_2O_4$ (K-DCA), with two bipyridine moieties and two carboxylate groups. The carboxylate- and pyridine-based active centers in K-DCA can reversibly react with four K-ions to provide a specific capacity of 163.3 mA h g^{-1} with a pair of redox plateaus centered at ~0.8 V. When coupling with nitrogen-doped reduced graphene oxide (NrGO), the composite anode material, K-DCA-NrGO, demonstrates a high specific capacity of 225.25 mA h g^{-1} and increased capacity retention during long-term cycling. Additionally, the reaction kinetics and mechanism studies demonstrate that the composite exhibits low overpotentials, low interphase resistance, a partial pseudo-capacitance behavior, and stable chemical/morphological structures upon cycling, which contribute to the fast kinetics and long cycle life.

1. Introduction

Li-ion batteries (LIBs) are the dominant energy storage devices in portable electronics, electric vehicles, and grid-scale stationary energy storage due to their high energy density and long cycle life. However, the large-scale applications of LIBs have triggered concerns about the scarcity, high cost, and toxicity of lithium and transition metal resources, as well as the recycling of spent LIBs. To address these challenges and satisfy the ever-growing demands for energy and environmental sustainability, K-ion batteries (KIBs) based on the abundant, low-cost, and highly sustainable potassium resources (2.09 wt% in the Earth's crust, 3.1 USD per kg *vs.* Li 0.0017 wt%, 19.2 USD per kg) attract considerable research interest.[1–5] Nevertheless, most inorganic electrode materials in LIBs and Na-ion batteries (NIBs) do not extend their high performance to KIBs due to the rigid crystalline structures and large volume changes caused by repeated insertion/de-insertion of K^+.[6–11] The ionic radius of K^+ (1.38 Å) is much larger than those of Na^+ (1.02 Å) and Li^+ (0.76 Å), resulting in a large volume change, severe particle pulverization, and fast capacity decay in KIBs upon long-term cycling.[12–23] To achieve high-performance and sustainable KIBs, developing novel electrode materials with stable and flexible structures to accommodate the large volume change and enable fast reaction kinetics is critical.

As universal electrode materials, organic electrode materials (OEMs) with abundant structural diversity and high structural flexibility have been extensively studied in alkali-ion batteries, and have exhibited exceptional performance in LIBs, which can be retained in KIBs. However, state-of-the-art OEMs still suffer from three challenges: (1) low electronic conductivity, which leads to sluggish reaction kinetics; (2) particle pulverization due to large volume changes during repeated K-ion insertion/de-insertion processes; (3) high solubility in the electrolyte, which results in fast capacity decay.[3,24–29] To overcome these challenges and obtain high-performance OEMs, molecular structure design and organic electrode engineering are of paramount importance. To reduce the solubility, salt formation is widely used because the formation of organic salts enhances the polarity and reduces the solubility of OEMs. To increase the conductivity and accommodate the large volume change, a highly conductive and large-surface-area host material such as graphene or porous carbon is used in organic electrodes to improve the reaction kinetics, mitigate particle pulverization, and further decrease the dissolution of OEMs in the electrolyte.[30–32] Compared with inorganic anode materials,[33,34] carboxylate-based anode materials have the advantages of low cost, abundance, high sustainability, and high structural tunability. Organic carboxylates are transition-metal free and can achieve high theoretical capacity by rational structural design. Compared with the other organic anode materials,[35] carboxylate-based anode materials have low redox potentials of <1 V, which make them ideal for developing high-performance anodes for KIBs.

[a] *Department of Chemistry and Biochemistry, George Mason University, Fairfax, VA, 22030, USA. E-mail: cluo@gmu.edu*
[b] *Quantum Science & Engineering Center, George Mason University, Fairfax, VA, 22030, USA*

† Electronic supplementary information (ESI) available. See DOI: https://doi.org/10.1039/d2nj03447f

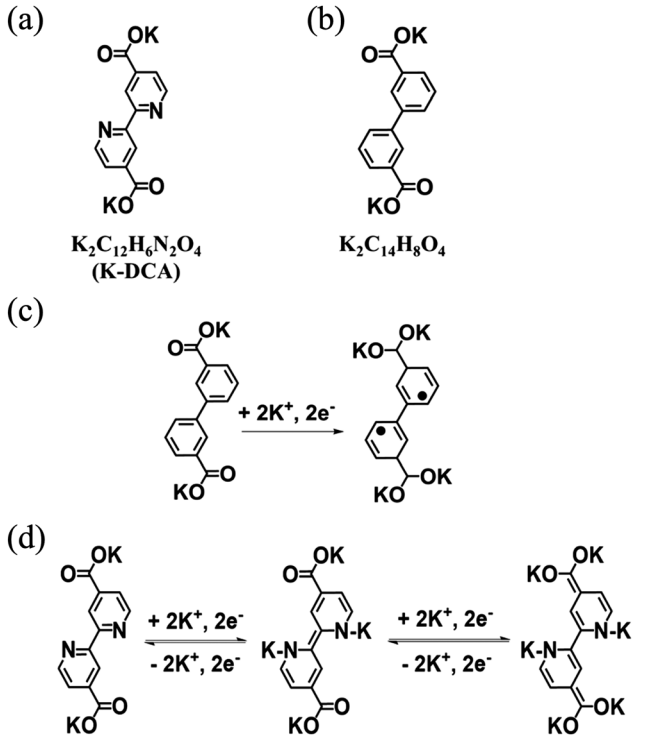

Scheme 1 The molecular structures of (a) $K_2C_{12}H_6N_2O_4$ (K-DCA) and (b) $K_2C_{14}H_8O_4$; (c) the proposed potassiation/de-potassiation mechanism of biphenyl-3,3′-dicarboxylic acid dipotassium salt ($K_2C_{14}H_8O_4$); (d) the proposed potassiation/de-potassiation mechanism of $K_2C_{12}H_6N_2O_4$ (K-DCA).

In this work, we present a novel N-containing carboxylate salt as an anode material for KIBs. Scheme 1a shows the molecular structure of the N-containing carboxylate salt, $K_2C_{12}H_6N_2O_4$ (K-DCA), consisting of two pyridine moieties and two carboxylate groups in the *meta* position. The presence of these two pyridine moieties increases the available active sites in K-DCA and provides resonance stability during K-ion insertion/de-insertion, resulting in the reversible four-electron/K^+ redox mechanism (Scheme 1d). As shown in Scheme 1b, a carboxylate salt without pyridine moieties (biphenyl-3,3′-dicarboxylic acid dipotassium salt, $K_2C_{14}H_8O_4$) was synthesized as a control. It is electrochemically inactive in KIBs and cannot reversibly react with K^+ and electrons (Scheme 1c), demonstrating the significant role of pyridine moieties in the electrochemical performance of the carboxylate anode. To optimize the electrochemical performance in KIBs, K-DCA was coupled with nitrogen-doped reduced graphene oxide (NrGO) and a 2.8 M KPF_6-DEGDME electrolyte. The K-DCA-NrGO anode exhibits exceptional electrochemical performance. This work demonstrates a promising organic anode material for developing next-generation green and sustainable energy storage devices.

2. Experimental procedure

2.1 Synthesis/preparation of electrode materials

2,2′-Bypyridine-4,4′-dicarboxylic acid dipotassium salt (K-DCA/$K_2C_{12}H_6N_2O_4$) was prepared as follows: 2,2′-bypyridine-4,4′-dicarboxylic acid (Alfa Aesar, 98%) was dispersed in ethanol with potassium hydroxide pellets (Sigma Aldrich, 85%) in 5% excess. The solution was stirred at room temperature for 24 hours; then the solution was filtered to collect the precipitate. The precipitate was washed with ethanol and dried in a vacuum oven at 90 °C overnight. The isolated product was a white powder.

2.2 Materials characterization

The active material, 2,2′-bypyridine-4,4′-dicarboxylic acid dipotassium salt (K-DCA/$K_2C_{12}H_6N_2O_4$), was spectroscopically analyzed *versus* the starting material, 2,2′-bypyridine-4,4′-dicarboxylic acid as proof of synthesis. Fourier transform infrared (FTIR) spectroscopy was recorded using an Agilent Cary 630 FTIR Spectrometer. Raman measurements were performed on a Horiba Jobin Yvon Labram Aramis using a 532 nm diode-pumped solid-state laser, attenuated to give a power of ~900 μW at the sample surface. Nuclear magnetic resonance (NMR) was recorded using a Bruker Ascend 400. Powder X-ray diffraction (PXRD) pattern was recorded using a Rigaku MiniFlex using CuKα radiation; and SEM images were taken using a Hitachi SU-70 analytical ultra-high-resolution SEM (Japan) and Joel JSM-IT500HR/LV high-resolution SEM.

2.3 Fabrication of electrodes and assembly of cells

The 2,2′-bypyridine-4,4′-dicarboxylic acid dipotassium salt (K-DCA/$K_2C_{12}H_6N_2O_4$) was mixed with carbon black (CB) and polyvinylidene fluoride (PVDF) binder to form a slurry with a weight ratio of 60 : 30 : 10. The electrode was prepared by casting the slurry onto copper foil using a doctor blade and drying in a vacuum oven at 90 °C overnight. The slurry coated on copper foil was punched into circular electrodes (K-DCA) with a mass loading of ~1.6 mg cm^{-2}. The mass loading of the active material in the K-DCA anode is ~0.96 mg cm^{-2}. Coin cells for K-ion batteries (KIBs) were assembled using potassium metal as the counter electrode, 2.8 M KPF_6 in diethylene glycol dimethyl ether (DEGDME) as electrolyte, and glass fiber (Whatman) as the separator.

The 2,2′-bypyridine-4,4′-dicarboxylic acid dipotassium salt (K-DCA/$K_2C_{12}H_6N_2O_4$) was mixed with nitrogen doped reduced graphene oxide (NrGO, ACS Material, LLC, single layer graphene, N-doped powder, 1 g) in a 2 : 1 ratio and ball-milled for 10 minutes. This subsequent mixture was then mixed with carbon black (CB) and polyvinylidene fluoride (PVDF) binder to form a slurry with a weight ratio of 80 : 10 : 10. The electrode was prepared by casting the slurry onto copper foil using a doctor blade and drying in a vacuum oven at 90 °C overnight. The slurry coated on copper foil was punched into circular electrodes (K-DCA-NrGO) with a mass loading of ~1.6 mg cm^{-2}. The mass loading of the active material in the K-DCA-NrGO anode is ~0.85 mg cm^{-2}. Coin cells for K-ion batteries (KIBs) were assembled using potassium metal as the counter electrode, 2.8 M KPF_6 in diethylene glycol dimethyl ether (DEGDME) as electrolyte, and glass fiber (Whatman) as the separator.

2.4 Electrochemical measurements

All galvanostatic discharge–charge cycles were performed using an Arbin battery testing instrument (Arbin Instrument, model LBT20084) at room temperature in a voltage range of 0.4–2.0 V. The cells were first discharged then recharged. Specific capacity is calculated based on the mass of the active material in the composite anode. Cyclic voltammograms (CVs) were recorded using a Gamry Reference 1010E Potentiostat/Galvanostat/ZRA at a scan rate of 0.1–1.0 mV s^{-1}. Impedance analysis was also performed using a Gamry Reference 1010E Potentiostat/Galvanostat/ZRA. CVs at various scan rates were used to study the reaction kinetics of K-DCA and K-DCA-NrGO anodes in KIBs. During the discharge/charge process, potassium ions get inserted into the anode and reversibly react with the two carboxylate groups at the *meta* position of the ring as well as the two nitrogens on the pyridine ring system, which is indicated in the potassiation/de-potassiation mechanism in Scheme 1d. Additionally, the K-DCA material consists of micro-sized particles ($\sim$1–5 μm) with aggregated nanorods clumped together, showing a high specific surface area. Hence, a partial capacitive behavior is exhibited due to monolayer adsorption of the ions at the electrode surface. In the GITT test, the battery was discharged to 0.4 V, and then charged back to 2 V at a current density of 20 mA g^{-1}. During the cycling process, the battery was discharged or charged for 30 min, and then rested for 6 h to reach the equilibrium potentials. To conduct the FTIR test before and after cycling, coin cells using K-DCA and K-DCA-NrGO, respectively, as the anode and potassium metal as the counter electrode were assembled. After cycling for 1, 10, and 20 cycles at 30 mA g^{-1}, the coin cells were disassembled in a glovebox. The cycled K-DCA and K-DCA-NrGO electrodes were washed using DEGDME and dried in a vacuum oven at 90 °C overnight. Then, the pristine and cycled electrodes were tested, and SEM images were taken using a Joel JSM-IT500HR/LV high-resolution SEM. For the PXRD and FTIR tests before and after cycling, thick electrodes were prepared by using polytetrafluoroethylene (PTFE) as the binder. K-DCA was mixed with NrGO in a 2 : 1 ratio and ball-milled for 10 minutes. This subsequent mixture was then mixed with CB and PTFE binder in a ratio of 80 : 10 : 10. A thick film was obtained directly after grinding the mixture for 20 minutes. After drying in a vacuum oven at 90 °C overnight, the thick electrodes were assembled in coin cells and cycled for 1, 10, and 20 cycles at 30 mA g^{-1}. The coin cells were disassembled in a glovebox and the cycled electrodes were washed using DEGDME and dried in a vacuum oven at 90 °C overnight. The pristine and cycled thick electrodes were tested using a Rigaku MiniFlex and Agilent Cary 630, respectively.

3. Results and discussion

The structure of the nitrogen-containing potassium carboxylate, K-DCA, was confirmed and characterized by X-ray powder diffraction (PXRD), Fourier-transform infrared (FTIR) spectroscopy, proton nuclear magnetic resonance (^{1}H NMR), carbon-13 nuclear magnetic resonance (^{13}C NMR), and scanning electron microscopy (SEM). The PXRD pattern of K-DCA in Fig. 1a (black) shows its crystalline structure, which is different from that of the precursor, DCA/$C_{12}H_8N_2O_4$ (Fig. S1a, ESI†). The FTIR spectrum of the carboxylate salt in Fig. 1b (black) shows the C═O asymmetric vibrational peaks at 1610 cm^{-1} and symmetric vibrational peaks at 1386 cm^{-1}. Compared with the FTIR spectrum of the precursor, DCA/$C_{12}H_8N_2O_4$ (Fig. S1b, ESI†), the FTIR spectrum of K-DCA (Fig. 1b, black) shows the disappearance of the peaks at 2428 cm^{-1} (O–H vibrations) and 1707 cm^{-1} (C═O, asymmetric vibrations on the benzene ring), indicating the complete conversion of the dicarboxylic acid to the potassium carboxylate salt. New peaks can be observed at 1610 cm^{-1} and 1386 cm^{-1}, corresponding to the asymmetrical and symmetrical vibrations of C═O in the carboxylates, respectively, while the peak at 1546 cm^{-1} corresponds to the vibrations of C═N in the pyridine moieties of K-DCA. Enlarged and labeled spectra are presented in Fig. S2a (ESI†). Raman spectroscopy was employed to further characterize NrGO, K-DCA, and the K-DCA-NrGO composite. In Fig. S2b (ESI†), NrGO shows two sharp peaks for the disordered carbon (D band) and the graphitic carbon (G band) at 1351 cm^{-1} and 1591 cm^{-1}, respectively, while K-DCA exhibits sharp peaks (Fig. S2c, ESI†) at 1610 cm^{-1} and 1412 cm^{-1}, representing the asymmetric and symmetric stretching vibrations of C═O in the carboxylate group. The sharp peak at 1554 cm^{-1} in Fig. S2c (ESI†) stands for the vibration of C═N in the pyridine moieties. The sloping baseline is ascribed to the fluorescence caused by the conjugated structure of K-DCA. In the spectrum of the K-DCA-NrGO composite (Fig. S2d, ESI†), the two sharp peaks for the D band and G band of NrGO are still present, while the peak intensity of K-DCA is weakened because of the encapsulation by NrGO. The sloping baseline can still be observed due to the presence of K-DCA in the composite. The Raman results confirm the structure of K-DCA and the K-DCA-NrGO composite. Further characterization studies of K-DCA using ^{1}H NMR (Fig. 1c) and ^{13}C NMR (Fig. 1d) with D_2O as the solvent were performed. In Fig. 1c, three ^{1}H NMR peaks in the range from 7.7–8.7 ppm represent the protons in the pyridine moieties of K-DCA, while no H signal from the unconverted dicarboxylic acid (at 13.846 ppm, Fig. S1c, ESI†), can be observed, demonstrating the successful formation of the potassium carboxylate. There is an obvious peak at 4.790 ppm, corresponding to the chemical shift of H in the D_2O solvent. The ^{13}C NMR spectrum of K-DCA (Fig. 1d) shows three peaks at 121.23 ppm, 123.23 ppm, and 149.61 ppm, corresponding to sp^2 carbons in the pyridine ring bonded with protons, while the peak at 146.30 ppm corresponds to sp^2 carbons in the pyridine ring bonded to the carboxylate groups. The ^{13}C NMR peak at 155.66 ppm corresponds to sp^2 carbons in the pyridine rings bonded to each other, while the ^{13}C NMR peak at 173.00 ppm corresponds to sp^2 carbons in the carboxylate groups. The surface morphology of the carboxylate was also investigated using SEM. It can be observed from Fig. 1e that K-DCA consists of short rod-like particles with the size of 1–5 μm. These characterization studies confirm the chemical structure and morphology of the N-containing carboxylate salt, K-DCA.

To investigate and confirm the effect of N in the ring system of K-DCA on the electrochemical performance in KIBs, a conjugated carboxylate compound similar to K-DCA but without N,

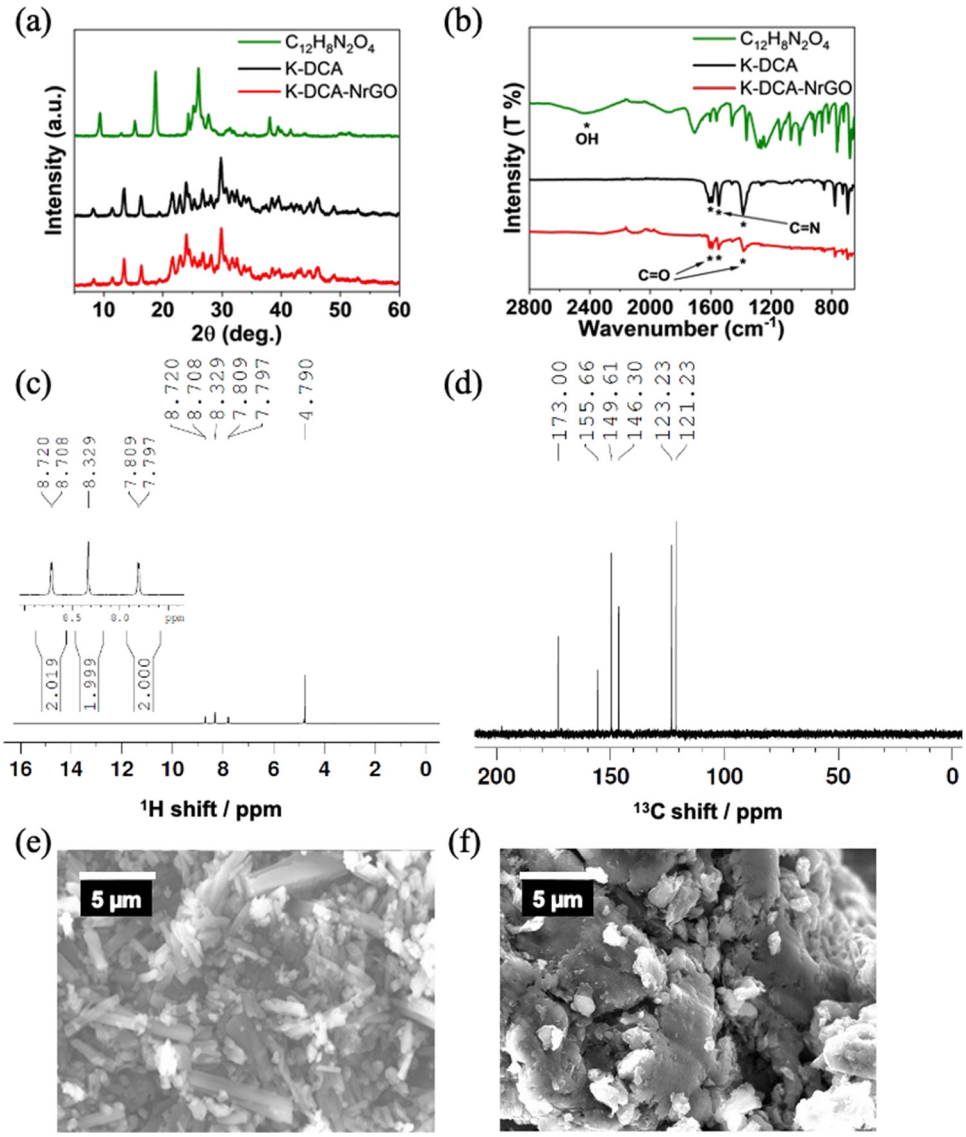

Fig. 1 Materials characterization of 2,2′-bypyridine-4,4′-dicarboxylic acid dipotassium salt (K-DCA) and 2,2′-bypyridine-4,4′-dicarboxylic acid dipotassium salt-NrGO (K-DCA-NrGO). (a) PXRD pattern; (b) FTIR spectrum; (c) ^{1}H NMR spectrum with a D_2O peak at 4.790 ppm; and (d) ^{13}C NMR spectrum, and SEM images with scale bars of 5 μm of (e) K-DCA and (f) K-DCA-NrGO.

was also synthesized as an anode material. The structure of the conjugated potassium carboxylate, $K_2C_{14}H_8O_4$, was confirmed and characterized by PXRD, FTIR, ^{1}H NMR, and ^{13}C NMR. The PXRD pattern in Fig. S3a (ESI†) indicates the crystalline structure of $K_2C_{14}H_8O_4$. The FTIR spectrum (Fig. S3b, ESI†) shows C═O asymmetric vibration peaks 1554 cm^{-1} and symmetric vibrational peaks at 1374 cm^{-1}. The ^{1}H NMR spectrum in Fig. S3c (ESI†) shows four peaks in the range from 7.5–8.3 ppm (two peaks overlapping at 7.8 and 7.9 ppm), representing the protons in the biphenyl moieties of $K_2C_{14}H_8O_4$. There is an obvious peak at 4.8 ppm, corresponding to the chemical shift of H in the D_2O solvent. The ^{13}C NMR spectrum in Fig. S2d (ESI†) shows four peaks at 127.26 ppm, 128.08 ppm, 129.06 ppm, and 137.02 ppm, corresponding to sp^2 carbons in the biphenyl ring bonded with protons, while the peak at 129.68 ppm corresponds to sp^2 carbons in the biphenyl ring bonded to the carboxylate groups. The ^{13}C NMR peak at 140.13 ppm corresponds to sp^2 carbons in the benzene rings bonded to each other, while the ^{13}C NMR peak at 175.36 ppm corresponds to sp^2 carbons in the carboxylate groups. The ^{1}H NMR and ^{13}C NMR spectra further confirm the chemical structure of $K_2C_{14}H_8O_4$, which was employed as a control to compare with K-DCA in KIBs.

To optimize the electrochemical performance of K-DCA in KIBs, it was paired with nitrogen-doped reduced graphene oxide (NrGO). Addition of the highly conductive NrGO is used to facilitate the electron and ion transfer of the anode, accommodate large volume changes during the repeated potassiation/de-potassiation processes, and form π–π interactions with K-DCA, thereby increasing its stability during long-term cycling. The resulting composite, K-DCA-NrGO, was also characterized using PXRD, FTIR, and SEM. The PXRD pattern in Fig. 1a (red) confirms that the crystalline structure of K-DCA (black) is

retained in the K-DCA-NrGO composite. The FTIR spectrum in Fig. 1b (red) of the composite material, K-DCA-NrGO, further confirms that the molecular structure of K-DCA is retained upon the addition of NrGO since the asymmetrical and symmetrical C=O vibrational peaks at 1610 cm^{-1} and 1386 cm^{-1} and C=N vibrational peak at 1546 cm^{-1} remain unchanged. The SEM image of K-DCA-NrGO (Fig. 1f) shows pulverized particles of K-DCA homogenously interspersed with NrGO sheets. These characterization studies confirm the chemical structure and morphology of the composite, K-DCA-NrGO.

The electrochemical performance of the K-DCA anode was evaluated using potassium metal as the counter electrode and 2.8 M KPF_6 DEGDME as the electrolyte. Fig. S4a (ESI†) shows the slopping charge/discharge curves with an average redox potential at ~0.8 V and a reversible capacity of 163.3 mA h g^{-1}. In the cyclic voltammetry (CV) result, a pair of cathodic peaks at ~0.5 V and ~0.9 V, as well as a pair of anodic peaks at ~0.45 V and ~0.8 V, is observed (Fig. S4b, ESI†), corresponding to the redox plateaus centered at ~0.8 V in Fig. S4a (ESI†). In the long-term cycling test (Fig. S4c, ESI†), a reversible capacity of 88 mA h g^{-1} at 50 mA g^{-1} was achieved and retained after 100 cycles, demonstrating moderate cycling stability and diminished capacity retention. The K-DCA anode suffers from rapid capacity loss, and its capacity decreases to below 100 mA g^{-1} after 30 cycles. The coulombic efficiency upon long-term cycling was >99%. The contribution of carbon black to the reversible capacity of the K-DCA anode was subsequently measured and found to exhibit a reversible capacity of 60 mA h g^{-1} (Fig. S5, ESI†). The rate capability of K-DCA (Fig. S4d, ESI†) was measured from 20 mA g^{-1}–2 A g^{-1}, and it demonstrated reversible capacities of 150.3 mA h g^{-1} and 40.6 mA h g^{-1}, respectively. After the current density reduces back to 20 mA g^{-1}, a reversible capacity of 103.2 mA h g^{-1} can be retained, demonstrating moderate reaction kinetics.

To fully investigate its performance and understand the effect of the pyridine moieties, potassium carboxylate, $K_2C_{14}H_8O_4$, without the pyridine moieties was also exploited as the anode material. As shown in Fig. S6a (ESI†), the galvanostatic charge/discharge curves of $K_2C_{14}H_8O_4$ exhibit a pair of sloping plateaus centered at ~0.7 V with a specific capacity of only 23 mA h g^{-1} (Fig. S6b, ESI†), which is contributed by the conductive carbon in the electrode. Hence, $K_2C_{14}H_8O_4$ is electrochemically inactive as an anode in KIBs. The evaluation and comparison of $K_2C_{14}H_8O_4$ and K-DCA demonstrate that the pyridine moieties play a critical role in the electrochemical performance of K-DCA in KIBs, allowing for a reversible four-electron/K^+ redox mechanism to occur.

To enhance the performance of DCA in KIBs, the K-DCA-NrGO composite was used as the anode active material with potassium metal as the counter electrode and 2.8 M KPF_6 in diethylene glycol dimethyl ether (DEGDME) as the electrolyte. The galvanostatic charge/discharge curves of K-DCA-NrGO are shown in Fig. 2a and exhibit one pair of redox plateaus centered at ~0.89 V with a reversible capacity of 225.3 mA h g^{-1}. The theoretical capacity of K-DCA is 335 mA h g^{-1} based on the four-electron reaction mechanism shown in Scheme 1d. The initial de-potassiation capacity of the K-DCA-NrGO anode achieved is lower than the theoretical capacity. This is ascribed to (1) the initial capacity loss triggered by the large volume change and organic material dissolution in the electrolyte; (2) the poor conductivity of the micro-sized K-DCA, which limits

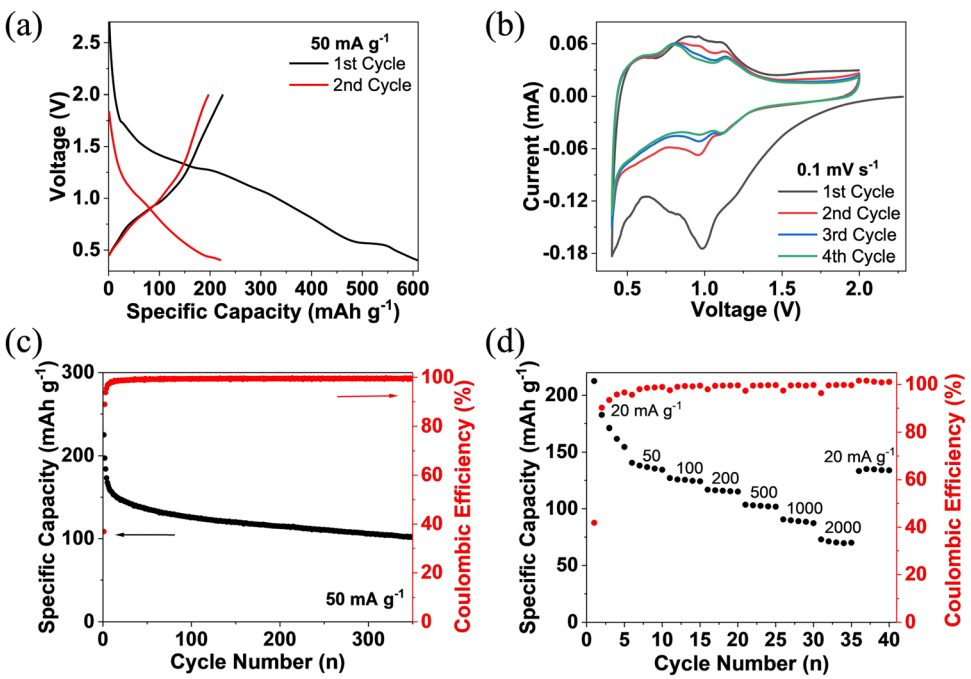

Fig. 2 Electrochemical performance of K-DCA-NrGO in KIBs. (a) Galvanostatic charge–discharge curves; (b) cyclic voltammograms at 0.1 mV s^{-1}; (c) de-potassiation capacity and coulombic efficiency *versus* cycle number at the current density of 50 mA g^{-1}; and (d) rate performance at various current densities.

material utilization; (3) the narrow cutoff window from 0.4 V to 2.0 V. Enlarging the cutoff window can increase the specific capacity at the price of worse cyclic stability. In the CV result, (Fig. 2b), a pair of cathodic peaks at ~0.7 V and ~1.1 V, and a pair of anodic peaks at ~0.8 V and ~1.1 V, are observed, corresponding to the redox plateaus centered at ~0.89 V, shown in Fig. 2a. In the long-term cycling test (Fig. 2c and Fig. S7, ESI†), reversible capacities of 115 mA h g^{-1} at 50 mA g^{-1} and 94 mA h g^{-1} at 200 mA g^{-1} were achieved and retained after 200 and 400 cycles, respectively, demonstrating excellent cycling stability and capacity retention. The coulombic efficiency of long-term cycling was >99%. However, the initial coulombic efficiency of the K-DCA-NrGO anode is low. The reasons are (1) the initial coulombic efficiency of carbon black and NrGO is low as shown in Fig. S5 and S8 (ESI†). This lowers the initial coulombic efficiency of the K-DCA-NrGO anode. (2) The anode was cycled in the cutoff window from 0.4 V to 2.0 V. A solid electrolyte interphase (SEI) will be generated in the initial cycles, which also lowers the initial coulombic efficiency of the K-DCA-NrGO anode. (3) The anode suffers from obvious initial capacity loss due to the large volume change and dissolution of K-DCA as shown in Fig. 2c and d. This further lowers the initial coulombic efficiency of the K-DCA-NrGO anode. The contribution of NrGO to the reversible capacity was subsequently measured and found to exhibit a reversible capacity of 71 mA h g^{-1} (Fig. S8, ESI†). The capacity loss of organic carboxylate anodes is due to the dissolution of the active material in the electrolyte and the large volume change caused by the repeated potassiation/de-potassiation processes. To address these challenges, we used nitrogen-doped reduced graphene oxide and a concentrated electrolyte in this work. Other methods can also be used to improve the long-term cycling stability. For example, various types of carbon materials such as microporous or mesoporous carbon can be used to confine the carboxylate compounds, which not only mitigates the dissolution of the active material in the electrolyte but also accommodates the volume change upon cycling. In addition, organic materials can be anchored to the carbon materials such as graphene or carbon nanotubes by covalent bonds, which chemically stabilize the active material and alleviate the capacity loss. Moreover, different types of electrolytes such as fluorinated electrolytes or gel electrolytes can be employed to improve the long-term cycling stability of the organic anode materials. As shown in Fig. 2e, rate capability of K-DCA-NrGO was measured from 20 mA g^{-1}–2 A g^{-1} and reversible capacities of 212.51 mA h g^{-1} and 72.98 mA h g^{-1}, respectively were demonstrated. After the current density reduces back to 20 mA g^{-1}, a reversible capacity of 133.38 mA h g^{-1} can be retained, demonstrating excellent reaction kinetics, thus confirming that the K-DCA-NrGO composite is a promising organic anode for KIBs.

To further explore the electrochemical properties and performance of K-DCA-NrGO in KIBs, CV, galvanostatic intermittent titration technique (GITT), and electrochemical impedance spectroscopy (EIS) were employed to study the reaction kinetics. In Fig. 3a, the K-DCA-NrGO anode was cycled at various scan rates from 0.1–1 mV s^{-1}; the resulting voltammograms show that peak

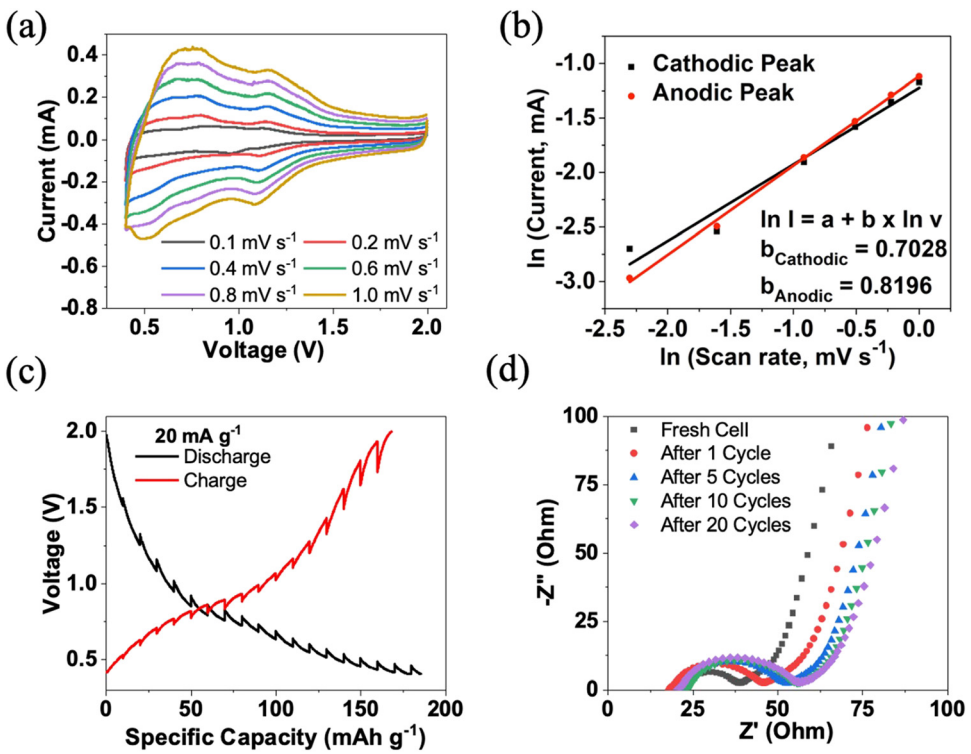

Fig. 3 Reaction kinetics of K-DCA-NrGO in KIBs. (a) Cyclic voltammograms at various scan rates; (b) the ln relationship of peak current and scan rate; (c) potential response during GITT measurements at 20 mA g^{-1}; and (d) impedance analysis before and after charge/discharge.

intensity increases at elevated scan rates. The linear fit of the natural logarithmic relationship of the scan rate and the peak current was evaluated and is presented in Fig. 3b and shows the cathodic and anodic slope (*b*) values of 0.7028 and 0.8196, respectively, indicating that the reaction kinetics of K-DCA-NrGO exhibits a partial pseudo-capacitive behavior, which contributes to its fast reaction kinetics. The equilibrium potentials obtained from GITT are shown in Fig. 3c and show that the charge/discharge equilibrium potentials of K-DCA-NrGO are centered at 1.0/0.6 V with overpotentials of 44 mV and 42 mV at the charge and discharge plateaus, respectively. These small overpotentials further confirm the fast reaction kinetics of K-DCA-NrGO. Additionally, EIS was employed to evaluate the impedance evolution of the K-DCA-NrGO anode upon cycling. As shown in Fig. 3d, the interfacial impedance of the fresh cell is ~18 ohms and slightly increases to ~28 ohms after 1 cycle. After 5, 10, and 20 cycles, the interfacial impedance was retained at ~34 ohms. The stable interfacial impedance from the 1st to 20th cycle demonstrates the stable SEI layer upon long-term cycling, which contributes to the stable cycle life. The CV, GITT, and EIS confirm the fast reaction kinetics and the formation of a stable SEI layer of the K-DCA-NrGO anode in KIBs.

In comparison, the reaction kinetics of the pure anode material, K-DCA, was also investigated by employing GITT and EIS. Presented in Fig. S9a (ESI†) are the equilibrium potentials obtained from GITT; they show the charge/discharge potentials remain centered at 1.0 V/0.6 V, respectively; however, the exhibited overpotentials (57 mV and 54 mV) are slightly larger than the overpotentials observed in the composite, K-DCA-NrGO, indicating that the addition of NrGO aides in improving the reaction kinetics of the anode material. EIS was additionally used to assess the impedance evolution of K-DCA upon cycling and is shown in Fig. S9b (ESI†); the interfacial impedance of the fresh cell is ~22 ohms and increases to ~71 ohms after 1 cycle.

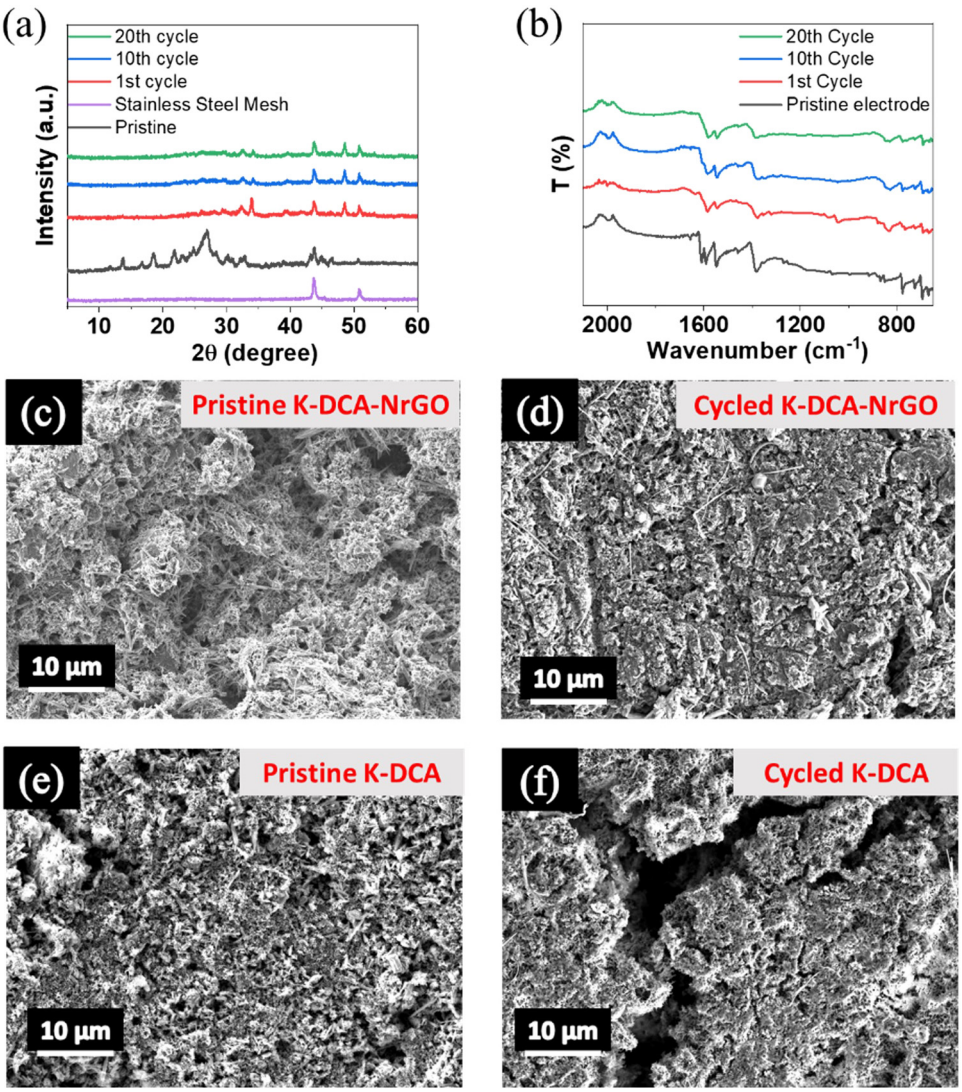

Fig. 4 Electrode characterization studies before and after cycling. (a) *Ex situ* PXRD patterns of pristine and cycled K-DCA-NrGO anodes; (b) FTIR spectra of pristine and cycled K-DCA-NrGO anodes; SEM images of (c) pristine K-DCA-NrGO anodes, (d) K-DCA-NrGO anodes after 20 cycles, (e) pristine K-DCA anodes, and (f) K-DCA anodes after 20 cycles.

With continued cycling the interfacial impedance continues to increase from ~60 Ohms after 5 cycles to ~67 ohms after 10 cycles, and ~76 ohms after 20 cycles. This indicates that the formation of the SEI layer in the pure K-DCA anode is not optimal, resulting in its rapid capacity loss and diminished cycle life. These results confirm that NrGO plays a critical role in improving the reaction kinetics and cyclic stability of K-DCA.

Additionally, to investigate the crystalline, molecular, or morphological structural change of the K-DCA-NrGO anode upon cycling, PXRD, FTIR, Raman, and SEM were employed. In Fig. 4a, the *ex situ* PXRD patterns for the pristine and cycled anodes show that the crystalline structure of K-DCA is changed after the first cycle, and the crystal structure becomes stable after the first cycle, indicating that the initial phase transformation is irreversible, and the newly formed crystalline structure is stable and reversible upon cycling. To examine any molecular structure changes resulting from cycling, FTIR was used. As shown in Fig. 4b, the FTIR peaks for the pristine and cycled K-DCA-NrGO do not show visible changes before and after cycling, demonstrating that the molecular structure of the both K-DCA and NrGO are retained after the potassiation/de-potassiation processes. Additionally, to explore and confirm the proposed redox mechanism, *ex situ* Raman was employed to confirm the active sites in K-DCA during the charge/discharge processes. Presented in Fig. S10 (ESI†), the *ex situ* Raman spectra show that the Raman peaks for the carbonyl group and pyridine group in K-DCA disappear when fully discharged to 0.4 V. Upon charging to 2 V, the carbonyl and pyridine peaks re-appear, demonstrating a reversible electrochemical reaction between the K ions and both the carbonyl and pyridine groups. Finally, SEM imaging was used to gain insight into the morphological changes of the pristine and cycled K-DCA-NrGO anodes. In Fig. 4c–f, SEM images show that small pores on the surface of the anodes (circled, measuring 3.626 μm) are created, as a result of large volume expansion, during repeated insertion/de-insertion of K ions during cycling. These morphology changes lead to the gradual capacity loss of the K-DCA-NrGO anode material during long-term cycling.

To compare with the K-DCA-NrGO anode, the pure K-DCA anode was also examined using FTIR and SEM to fully understand the stabilizing effects of NrGO upon cycling. In Fig. S11 (ESI†), the FTIR spectra of pristine and cycled K-DCA anodes do not show significant changes before and after cycling, demonstrating that the molecular structure of the pure anode material is stable. To understand the morphological changes resulting from cycling, SEM was employed to examine the surface morphology of pristine and cycled K-DCA anodes and the results are presented in Fig. 4e and f. These anodes show that large cracks, circled and measuring 5.409 μm (top) and 5.432 μm (bottom), are generated on the anode surface after 20 cycles. These obvious and extreme morphology changes are caused by the repeated potassiation/de-potassiation processes which lead to the capacity loss observed during long-term cycling of K-DCA (Fig. S4c, ESI†). These results confirm that while the molecular structure of K-DCA is stable upon cycling, the morphology changes caused by the volume expansion/shrinkage during the repeated potassiation/de-potassiation processes result in a significant capacity loss. Therefore, these results further confirm that the highly conductive NrGO is critical to improve the electrochemical performance of the organic anode, K-DCA, in KIBs.

To design redox-active carboxylate compounds, two or more carboxylate groups should be connected by a fully conjugated structure, consisting of strictly alternating carbon–carbon double and single bonds. However, when reacting with K ions, $K_2C_{14}H_8O_4$ will generate an unstable radical intermediate rather than a stable product (Scheme 1b), so the reaction is irreversible, and $K_2C_{14}H_8O_4$ is electrochemically inactive. To activate the carboxylate groups in $K_2C_{14}H_8O_4$, the carbons on the *para* position of the benzene rings can be replaced by N to create extra active centers to alter the conjugation structure. For instance, K-DCA with N on the *para* positions contains four active centers, which are two carboxylate groups and two N in the pyridine moieties. The two N in the pyridine moieties first react with K^+ and electrons, and this triggers the rearrangement of the carbon–carbon double and single bonds (Scheme 1d), which reconnects the two carboxylate groups by a fully conjugated structure for further potassiation/de-potassiation reaction. All the active centers in K-DCA are connected by strictly alternating carbon–carbon double and single bonds during the redox reaction, and K-DCA demonstrates a promising organic anode as evidenced in this work. Further structure design on the carbon in the *para* position of the benzene ring can be made. For example, other redox-active groups such as carboxylate, cyano, thiocarboxylate, *etc.* can be introduced into that position to create extra active centers and alter the conjugation structure for high-capacity and low-voltage organic carboxylate anodes in KIBs.

4. Conclusions

This work investigates a new N-containing carboxylate salt, K-DCA, with two carboxylate groups and two pyridine moieties. With the assistance of highly conductive and large-surface-area NrGO, the K-DCA-NrGO anode exhibits exceptional electrochemical performance in terms of high cycle stability and robust reactions kinetics in KIBs. Our work proves that NrGO aids in enhancing the electrode conductivity, decreasing active material dissolution through π–π interactions with K-DCA, and accommodating large volume changes during the repeated potassiation/de-potassiation processes. CV, GITT, and EIS analyses confirmed excellent reaction kinetics and the formation of a stable SEI layer, contributing to the good cycle life. While PXRD and FTIR analyses of pristine and cycled anodes further confirmed the formation of a stable crystalline structure after the first cycle and stable molecular structures upon cycling, *ex situ* Raman analysis confirmed the four-electron K^+ redox mechanism. This work proves the application and viability of K-DCA-NrGO as an anode material for sustainable K-ion batteries and opens opportunities for its continued investigation as a universal anode material for other battery systems.

Conflicts of interest

The authors declare no competing interests.

Acknowledgements

This work was supported by the US National Science Foundation (NSF) Award No. 2154145. The authors acknowledge the support from George Mason University Chemistry & Biochemistry Department and the George Mason University Quantum Science & Engineering Center.

References

1 C. P. Grey and J. M. Tarascon, *Nat. Mater.*, 2016, **16**, 45–56.
2 J. Piątek, S. Afyon, T. M. Budnyak, S. Budnyk, M. H. Sipponen and A. Slabon, *Adv. Energy Mater.*, 2021, **11**, 2003456.
3 K. Holguin, M. Mohammadiroudbari, K. Qin and C. Luo, *J. Mater. Chem. A*, 2021, **9**, 19083–19115.
4 Y. Liang, C. Luo, F. Wang, S. Hou, S.-C. Liou, T. Qing, Q. Li, J. Zheng, C. Cui and C. Wang, *Adv. Energy Mater.*, 2018, **9**, 1802986.
5 W. Zhang, W. Huang and Q. Zhang, *Chem. – Eur. J.*, 2021, **27**, 6131.
6 B. Wang, Y. Han, X. Wang, N. Bahlawane, H. Pan, M. Yan and Y. Jiang, *iScience*, 2018, **3**, 110–133.
7 L. Xue, Y. Li, H. Gao, W. Zhou, X. Lü, W. Kaveevivitchai, A. Manthiram and J. B. Goodenough, *J. Am. Chem. Soc.*, 2017, **139**, 2164–2167.
8 C. Zhang, Y. Xu, M. Zhou, L. Liang, H. Dong, M. Wu, Y. Yang and Y. Lei, *Adv. Funct. Mater.*, 2017, **27**, 1604307.
9 Y.-H. Zhu, X. Yang, D. Bao, X.-F. Bie, T. Sun, S. Wang, Y.-S. Jiang, X.-B. Zhang, J.-M. Yan and Q. Jiang, *Joule*, 2018, **2**, 736–746.
10 J. Liao, Q. Hu, X. He, J. Mu, J. Wang and C. Chen, *J. Power Sources*, 2020, **451**, 227739.
11 Z. Zhang, M. Li, Y. Gao, Z. Wei, M. Zhang, C. Wang, Y. Zeng, B. Zou, G. Chen and F. Du, *Adv. Funct. Mater.*, 2018, **28**, 1802684.
12 J. Han, G.-N. Li, F. Liu, M. Wang, Y. Zhang, L. Hu, C. Dai and M. Xu, *Chem. Commun.*, 2017, **53**, 1805–1808.
13 J. H. Jo, J. U. Choi, Y. J. Park, Y. H. Jung, D. C. Ahn, T. Y. Jeon, H. S. Kim, J. Kim and S. T. Myung, *Adv. Energy Mater.*, 2020, **10**, 1903605.
14 H. Kim, J. C. Kim, S. H. Bo, T. Shi, D.-H. Kwon and G. Ceder, *Adv. Energy Mater.*, 2017, **7**, 1700098.
15 T. Masese, K. Yoshii, M. Kato, K. Kubota, Z. D. Huang, H. Senoh and M. Shikano, *Chem. Commun.*, 2019, **55**, 985–988.
16 H. Zhang, K. Xi, K. Jiang, X. Zhang, Z. Liu, S. Guo and H. Zhou, *Chem. Commun.*, 2019, **55**, 7910–7913.
17 X. Wu, D. P. Leonard and X. Ji, *Chem. Mater.*, 2017, **29**, 5031–5042.
18 Y. Liu, Y.-X. Lu, Y.-S. Xu, Q.-S. Meng, J.-C. Gao, Y.-G. Sun, Y.-S. Hu, B.-B. Chang, C.-T. Liu and A.-M. Cao, *Adv. Mater.*, 2020, **32**, 2000505.
19 X. Q. Chang, X. L. Zhou, X. W. Ou, C.-S. Lee, J. Zhou and Y. Tang, *Adv. Energy Mater.*, 2019, **9**, 1902672.
20 B. Ji, F. Zhang, N. Wu and Y. Tang, *Adv. Energy Mater.*, 2017, **7**, 1700920.
21 H. B. Ding, J. Wang, L. Fan, Z. Liu, X. Jia, X. Yu and B. Lu, *Chem. Eng. J.*, 2020, **395**, 125147.
22 H. Huang, J. Wang, X. Yang, R. Hu, J. Liu, L. Zhang and M. Zhu, *Angew. Chem., Int. Ed.*, 2020, **59**, 14693.
23 M. Wang, W. Lu, H. Zhang and X. Li, *Trans. Tianjin Univ.*, 2021, **27**, 1–23.
24 J. Heiska, M. Nisula and M. Karppinen, *J. Mater. Chem. A*, 2019, **7**, 18735–18758.
25 S. Xu, Y. Chen and C. Wang, *J. Mater. Chem. A*, 2020, **8**, 15547.
26 S. Muench, A. Wild, C. Friebe, B. Häupler, T. Janoschka and U. S. Schubert, *Chem. Rev.*, 2016, **116**, 9438–9484.
27 Z. Song and H. Zhou, *Energy Environ. Sci.*, 2013, **6**, 2280–2301.
28 C. Luo, Y. Zhu, Y. Xu, Y. Liu, T. Gao, J. Wang and C. Wang, *J. Power Sources*, 2014, **250**, 372–378.
29 H. Wu, S. A. Shevlin, Q. Meng, W. Guo, Y. Meng, K. Lu, Z. Wei and Z. Guo, *Adv. Mater.*, 2014, **26**, 3338–3343.
30 M. Lee, J. Hong, H. Kim, H.-D. Lim, S. B. Cho, K. Kang and C. B. Park, *Adv. Mater.*, 2014, **26**, 2558–2565.
31 X. Fan, F. Wang, X. Ji, R. Wang, T. Gao, S. Hou, J. Chen, T. Deng, X. Li, L. Chen, C. Luo, L. Wang and C. Wang, *Angew. Chem., Int. Ed.*, 2018, **57**, 7146–7150.
32 J. Hong, M. Lee, B. Lee, D.-H. Seo, C. B. Park and K. Kang, *Nat. Commun.*, 2014, **5**, 5335.
33 B. John, V. Anoopkumar and T. D. Mercy, *ACS Appl. Energy Mater.*, 2020, **3**, 9478–9492.
34 C. H. Jo, J. H. Jo, J. U. Choi, H. Yashiro, H. Kim and S. T. Myung, *ACS Sustainable Chem. Eng.*, 2020, **8**, 3743–3750.
35 M. Zhang, W. Huang, Q. Huang, X. Yu, J. Wu, S. Di, H. Ye, Y. Wu and Y. Li, *Energy Fuels*, 2021, **35**, 20367–20373.

